



Crustal origin of trench-parallel shear-wave fast polarizations in the Central Andes



I. Wölbern*, U. Löbl, G. Rümpler

Institute of Geosciences, Goethe University Frankfurt, Altenhöferallee 1, 60438 Frankfurt am Main, Germany

ARTICLE INFO

Article history:

Received 22 July 2013

Received in revised form 11 February 2014

Accepted 13 February 2014

Available online 6 March 2014

Editor: P. Shearer

Keywords:

Central Andes

subduction zone

seismic anisotropy

shear-wave splitting

FD modeling

ABSTRACT

In this study, SKS and local S phases are analyzed to investigate variations of shear-wave splitting parameters along two dense seismic profiles across the central Andean Altiplano and Puna plateaus. In contrast to previous observations, the vast majority of the measurements reveal fast polarizations sub-parallel to the subduction direction of the Nazca plate with delay times between 0.3 and 1.2 s. Local phases show larger variations of fast polarizations and exhibit delay times ranging between 0.1 and 1.1 s. Two 70 km and 100 km wide sections along the Altiplano profile exhibit larger delay times and are characterized by fast polarizations oriented sub-parallel to major fault zones. Based on finite-difference wavefield calculations for anisotropic subduction zone models we demonstrate that the observations are best explained by fossil slab anisotropy with fast symmetry axes oriented sub-parallel to the slab movement in combination with a significant component of crustal anisotropy of nearly trench-parallel fast-axis orientation. From the modeling we exclude a sub-lithospheric origin of the observed strong anomalies due to the short-scale variations of the fast polarizations. Instead, our results indicate that anisotropy in the Central Andes generally reflects the direction of plate motion while the observed trench-parallel fast polarizations likely originate in the continental crust above the subducting slab.

© 2014 Elsevier B.V. All rights reserved.

1. Introduction

Seismic anisotropy provides a unique link between the splitting of shear-waves into orthogonally polarized fast and slow components and deformation processes within the earth. It is often interpreted in terms of strain-induced crystallographic preferred orientation (CPO – sometimes also referred to as lattice preferred orientation, LPO) of mineral fabric due to flow fields (Long and Silver, 2009a; Savage, 1999; Buttle and Olson, 1998; Rabbel et al., 2013) or in terms of shape preferred orientation (SPO) due to sub-parallel structures such as stress-induced cracks or fine alternating layers (Park and Levin, 2002; Leidig and Zandt, 2003; Hammond et al., 2010; Buontempo and Wuestefeld, 2012). One of the major constituents of the Earth's mantle, olivine, tends to align under most conditions of deformation with the fast axis sub-parallel to the shear direction, i.e. sub-parallel to the plate motion (Long and Silver, 2009a; Savage, 1999). However, previous studies worldwide have shown that fast polarizations above subduction zones are often oriented perpendicular to the direction of slab movement (Russo and Silver, 1994; Long and Silver, 2008, 2009b; Hanna and Long, 2012; Lynner and Long, 2013). Other studies have

reported variations from trench-parallel directions in the fore arc to trench-normal orientations in the back-arc region (Tono et al., 2009; Fischer et al., 2000; Liu et al., 2008). These observations have been explained by models of trench-parallel mantle flow beneath the subducting slabs induced by trench rollback (Long and Silver, 2008, 2009b) or slab geometry (Russo and Silver, 1994; Kneller and van Keken, 2007; Di Leo et al., 2012).

Alternative explanations emanate from mineralogical constraints. Olivine can develop different CPOs depending on water content, pressure, and shear stress conditions (Jung and Karato, 2001; Jung et al., 2009; Katayama and Karato, 2006; Ohuchi et al., 2011). The prevalent A-type fabric (with the (010)[100] slip system as described above) forms in dry olivine under low stress conditions. In water-rich mantle, however, the B-type fabric (with the (010)[001] slip system) can develop when the shear stress is high or when the temperature is rather low. Such conditions are expected in subduction zones. This slip transition is expressed in a rotation of the fast-axis orientation perpendicular to the plate motion. Ohuchi et al. (2012) have further demonstrated that the existence of B-type olivine is most likely restricted to the fore-arc region of the mantle wedge, where water is released from the subducting slab. Serpentine is another highly anisotropic mineral that is likely to occur in subduction zones. Faccenda et al. (2008) suggest that the slab significantly

* Corresponding author. Tel.: +49 (0)69 79840139; Fax: +49 (0)69 79840131.

E-mail address: woelbern@geophysik.uni-frankfurt.de (I. Wölbern).

contributes to SKS splitting due to a combination of CPO and SPO originating from aligned sub-vertical fluid-filled cracks and serpentinized rocks. Serpentine is also present in the hydrated mantle wedge above the slab, where it also likely develops CPO as a consequence of mantle flow. The resulting serpentine fabric would also contribute with a fast-axis component perpendicular to the flow direction, i.e. sub-parallel to the trench (Katayama et al., 2009; Jung, 2011).

The Nazca–South American margin was one of the first subduction zones where seismic anisotropy has been investigated in greater detail. Russo and Silver (1994) have reported dominant fast axes of trench-parallel orientations with the exception of three confined zones where trench-normal alignments prevail. One of which was interpreted as a stagnation point in the center of the sub-slab mantle flow towards the north and the south while the other two zones coincide with changes of the slab dip influencing the flow field. This interpretation was derived, to a large degree, from investigations of source-side S-wave splitting based on a rather sparse set of intra-slab earthquakes. The corresponding ray paths were, thus, restricted to the sub-slab mantle. The analysis of SKS and local S phases (Polet et al., 2000) recorded at three different temporary networks indicated the existence of a zone, between 18°S and 20°S, where fast axes are predominantly oriented EW, while trench-parallel directions were reported north and south of this area. In the study presented here, we analyze data recorded as part of the ReFuCA project (Heit et al., 2008; Wölbern et al., 2009) along two EW oriented profiles in the Central Andes. From SKS and local S phases splitting parameters are determined to investigate short-scale lateral variations of anisotropy patterns from the Pacific coast near the trench towards the interior of the South American continent. The results are used to test a series of 2D anisotropic subduction zone models to evaluate the effects of different anisotropic zones on the shear-wave propagation and to discriminate between contributions from the mantle and the crust.

2. Shear-wave splitting analysis

2.1. Data and method

Within the ReFuCA project seismic stations were operated along two EW aligned profiles from March 2002 until January 2004. The northern profile at 21°S ranges from the Pacific coast to the Bolivian Interandean Zone while the southern profile transects the Puna plateau at 25.5°S (Fig. 1). The profiles extend over distances of ~600 km and ~200 km, respectively, with an average station spacing of ~10 km (Heit et al., 2008; Wölbern et al., 2009). We investigate SKS phases of events at distances $\geq 85^\circ$ with magnitudes ≥ 6.5 and further analyze local S phases from events within the Nazca slab with magnitudes ≥ 4.5 and focal depths between 150 and 350 km unless the incidence angle exceeds 30° at the recording station. Based on these criteria we have extracted SKS phases from seven events and also S phases from seven local events of sufficient quality from the ReFuCA data. Source parameters of the selected events are listed in the Supplementary Table S1.

We use a transverse-component minimization method (Silver and Chan, 1991; Rümpler and Silver, 1998; Long and Silver, 2009a) to investigate the shear-wave splitting. At first, seismograms are rotated into the RT coordinate system. A grid-search approach is utilized to find the pair of splitting parameters Φ and δt that best minimizes the energy on the transverse component. This is equivalent to the linearization of the particle motion. Uncertainties are estimated from the extent of the 95% confidence region of the splitting parameters determined from the transverse-component energy (Silver and Chan, 1991). For this purpose we have adopted the corresponding routines of the SplitSlab software

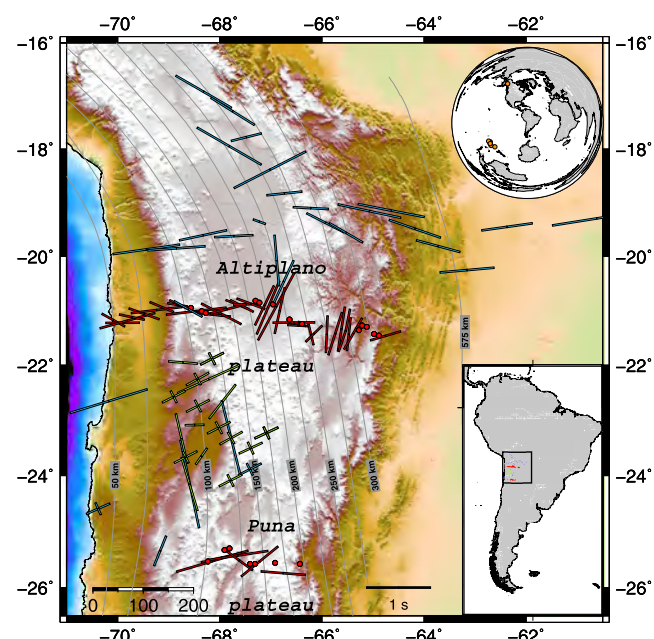


Fig. 1. Splitting parameters obtained from SKS phases. Bars denote orientations of apparent shear-wave fast polarization Φ with the length referring to the delay time δt (see scale at the bottom). Red bars display the new results of our study obtained from a joint-splitting analysis of the ReFuCA data. Dots denote null measurements obtained from joint-splitting. Green bars refer to reprocessed data from the PISCO experiment (Bock et al., 1998) also derived from joint-splitting analysis where applicable. Blue bars illustrate results and errors directly taken from a previous study (Polet et al., 2000). Green and blue crosses mark null measurements with the long bars indicating the orientation of initial polarization. Grey contour lines give the depths to the subducting Nazca slab as derived from local seismicity (Cahill and Isack, 1992). The inset in the upper right corner displays the locations of teleseismic events used in the SKS analysis.

package (Wüstefeld et al., 2008). For the SKS phases we use a bandpass in a frequency range from 0.02 Hz to 0.25 Hz and for the local S phases a frequency range from 0.02 Hz to 1 Hz. In principle, SKS phases are affected by anisotropy of the entire mantle beneath the receiver, whereas local slab events will be mainly affected by anisotropy within the mantle wedge and the overriding plate.

So-called “null” measurements either indicate the absence of anisotropy along the ray path or the alignment of the fast or slow axis of the anisotropic medium with the initial polarization of the observed phase (Long and Silver, 2009a; Hanna and Long, 2012). Alternatively, null measurements can be obtained in the case of two horizontal layers, e.g. if the fast axes orientations differ by 90° , such as a transition from A-type to B-type olivine in the same flow field. The initial polarization of the SKS phase is readily known from the backazimuth of the event location, but we also derive the initial polarization independently from the long-period fraction ($T > 15$ s) of the waveform in order to account for possible misalignments of horizontal components at the stations. The initial polarization of local S phases is determined directly from the long-period particle motion with $T > 5$ s (Rümpler and Silver, 1998).

Event-station pairs with incidence angles $\geq 30^\circ$ have been discarded from the study, because shear phases may be affected by nonlinear particle motion if the incidence angle exceeds $\sim 35^\circ$ at the surface (Long and Silver, 2009a; Savage, 1999). It is a frequent problem that Φ and δt determined with this method are sensitive to the selected shear-wave window (Teauby et al., 2004), most likely due to interfering phases or noise. Splitting parameters are, therefore, repeatedly analyzed for a number of randomly selected time windows enclosing the SKS or S wavelet in order to test for

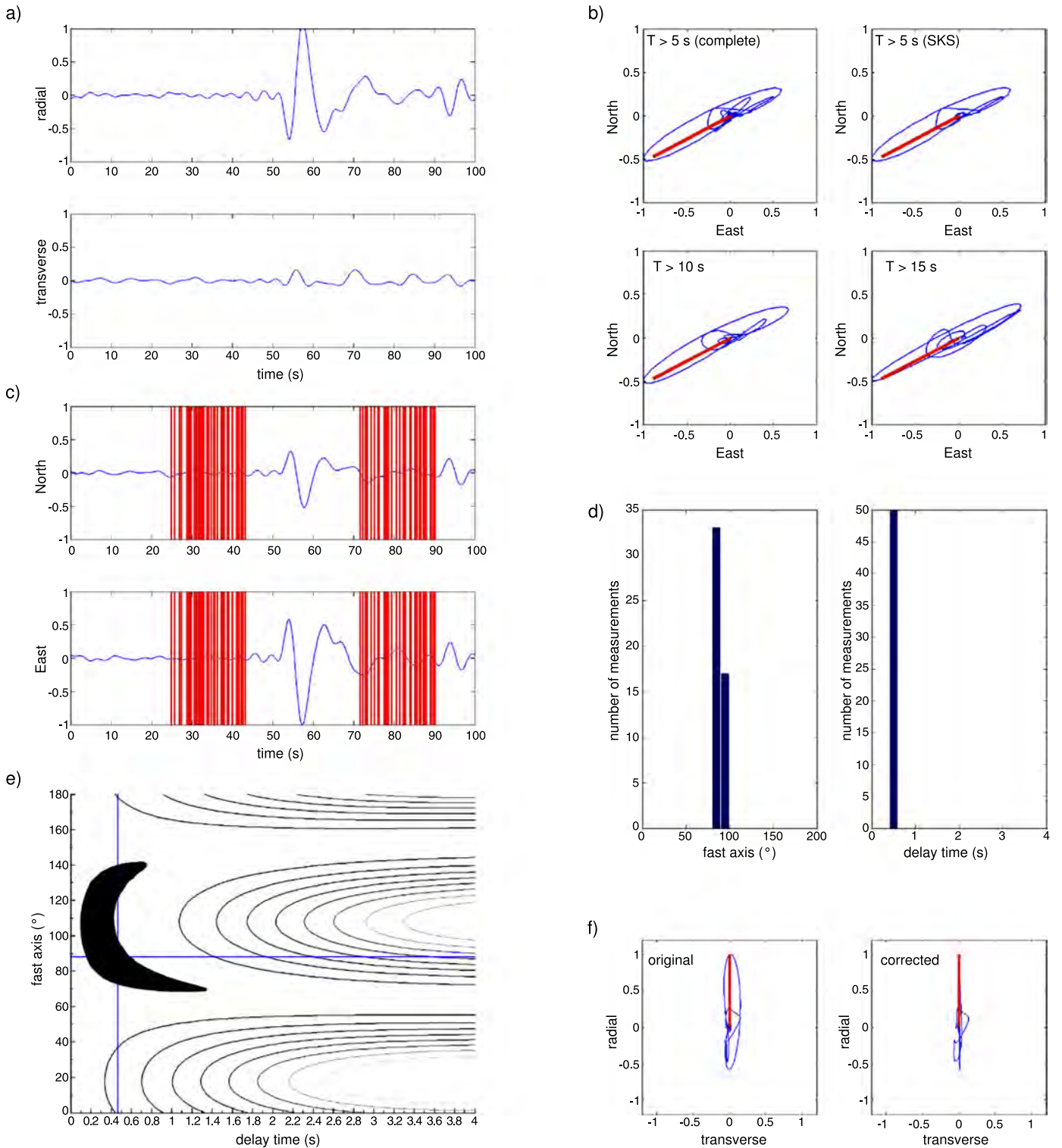


Fig. 2. Illustration of the SKS splitting analysis for an event recorded at station RF12. (a) Radial and transverse component of the data example. The energy on the transverse component is weak but significantly above the noise level. (b) The horizontal particle motion at different periods. The red bar indicates the orientation of the initial polarization which concurs with the backazimuth of the event. (c) Original North and East components with the red bars illustrating the random selection of fifty time windows for repeated analysis. (d) The distribution of splitting parameters obtained from each of the measurements. (e) The transverse-component energy obtained from the grid-search of splitting parameters. The thin blue crossed lines mark the splitting parameters that best minimize the energy on the transverse component averaged over fifty measurements. The black area refers to the related 95% confidence region. (f) The linearization of the particle motion after correction (right) compared to the original (left).

the robustness of the measurement. A data example illustrates the analysis (Fig. 2). An example of local S-phase analysis is shown in the Supplementary Fig. S1. If the analysis results in a bimodal distribution of fast polarizations the events are discarded from further analysis.

At stations that provide more than one event with suitable SKS phases we apply a joint-splitting analysis (Homuth, 2010), i.e. splitting parameters Φ and δt are determined in the grid-search approach that simultaneously minimizes the total energy of the transverse components from all related events. This is approxi-

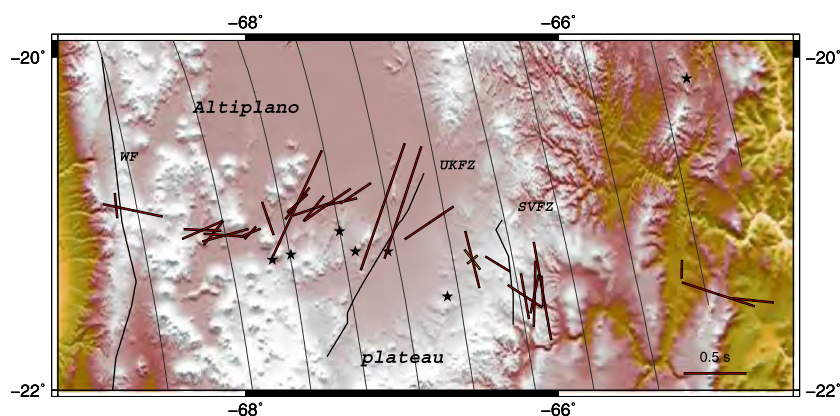


Fig. 3. Splitting parameters along the northern ReFuCA profile in the Altiplano plateau from local S phases. Results refer to single events. Splitting parameters are illustrated as described in Fig. 1. A different scaling is used to account for smaller delay times δt . Black asterisks mark the epicenters of earthquakes used in this study. At several stations fast polarizations align sub-parallel to the direction of major fault-zones as depicted by back lines. WF: West Fissure; UKFZ: Uyuni–Kenayani fault zone; SVFZ: San Vicente fault zone (Elger et al., 2005; ANCORP Working Group, 2003).

mately equivalent to the stacking method developed by Vinnik et al. (1989) and modified by Wolfe and Silver (1998) and Restivo and Helffrich (1999), except that we directly analyze the total transverse energy instead of eigenvalues. Our approach is implemented by extracting and concatenating the selected time windows from all related events. The joint-splitting analysis effectively reduces the influence of noise on the splitting analysis, because the total amount of energy for all events at one station is minimized simultaneously in the grid-search procedure. The method also increases the robustness of the splitting analysis in the case of low energy on all transverse components. The efficient linearization of the particle motions (Supplementary Fig. S2) corroborates the reliability of the joint analysis. Uncertainties are again estimated from the 95% confidence level (Supplementary Fig. S3). If the merged transverse component completely lacks of significant energy above the noise level the joint analysis will result in a null measurement.

The joint-splitting analysis is not applicable, however, if the splitting parameters at a given station vary significantly with backazimuth. In such cases the joint-splitting analysis results in an insufficient linearization of the particle motions. Variations as a function of backazimuth, i.e. as a function of initial polarization, can be caused, e.g., by vertical changes of anisotropic properties (Savage, 1999; Rümpker and Silver, 1998). All of the SKS waveforms used for this study arrive from a similar backazimuth ($\sim 240^\circ$) or from a direction perpendicular ($\sim 330^\circ$) to it, so that the joint-splitting analysis is applicable. An insufficient linearization of particle motion in this case can still result from a distortion of the analyzed waveform due to interfering phases. The corresponding events have been discarded from the grid search. Fast-axis orientations obtained from the joint splitting analysis are usually in good agreement with the results from single events. In the following we focus on the results from the joint-splitting analysis. However, the joint-splitting analysis is not applied to local S phases because the initial polarizations strongly differ along the profile.

2.2. Results

Fast polarizations obtained from SKS phases along the northern ReFuCA profile are predominantly oriented EW (red bars in Fig. 1; detailed results in Supplementary Table S2). In the middle of the profile, i.e. in the Altiplano plateau, we observe a well-defined corridor of about 50 km width, where orientations change abruptly towards NE–SW directions. Further east, a second anomaly of ~ 100 km width is located in the Eastern Cordillera, where the fast polarization turns towards NE–SW again. Corresponding delay times vary between 0.3 and 1.2 s and the largest delay times

are associated with NE–SW orientations of the Altiplano anomaly. Along the southern profile null measurements dominate the analysis of individual SKS events, however initial polarizations of the events are generally found to be oriented almost parallel or perpendicular to the fast polarizations obtained for that region. The joint analysis is also dominated by null measurements, however, it also reveals fast-polarization directions (red bars in Fig. 1; detailed results in Supplementary Table S3) at other locations which are consistent with the few results obtained from single-event analysis. This likely indicates that individual null measurements are due to the alignment of initial polarization with the fast axis of anisotropy rather than due to isotropic elastic properties. Orientations are roughly similar to the northern profile with prevailing EW directions. The delay times are slightly larger on average, but do not exceed 1.2 s.

Results from a previous study (Polet et al., 2000, blue bars in Fig. 1) also show EW fast-polarization directions along a profile at $\sim 20^\circ$ S and further north with a tendency to more trench-parallel orientations north of 18° S. The same study reports NS directions south of 23° S. Their results agree well with our observations along the Altiplano profile: one station directly collocates with a station on the ReFuCA profile near the western edge of the volcanic arc; it reveals the same EW fast polarization while two other stations north of the profile reflect the same anomalous NS trending fast polarization that we observe at stations in the Altiplano plateau. We have further re-processed additional data from the PISCO experiment (Bock et al., 1998) which covers the transition from the Altiplano to the Puna plateau (green bars in Fig. 1, see Supplementary Table S4 for detailed results). The majority of the PISCO stations reveal null measurements with the initial polarization sub-parallel to NE–SW trending fast polarizations obtained at three stations in the same area. Two locations show EW orientations of the fast polarization while the other two remaining stations are oriented NS. Delay times range from 0.3 to 1.1 s. Summarizing all new and previous SKS splitting results we observe a majority of fast directions sub-parallel to the Nazca plate motion throughout a latitude range from 18° S to at least 25.5° S (Fig. 4a). Trench-parallel orientations are scarce and seem to represent local or regional anomalies. Our results are in contrast to the large delay times reported from source-side splitting (Russo and Silver, 1994). A possible source for the disagreement may arise from the source-side splitting technique: the receiver-side splitting must be known accurately to isolate the source-side effects (Lynner and Long, 2013). However, the receiver side splitting may be difficult to characterize by a single pair of splitting parameters, e.g. in the case of layered anisotropy

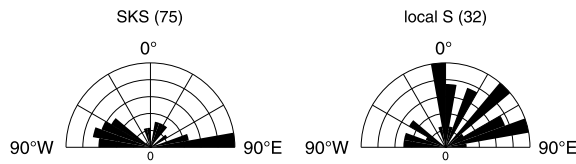


Fig. 4. Comparison of fast-polarization orientations for teleseismic and local events. The number of related measurements are given in brackets. (a) Fast polarizations obtained from SKS phases including results from previous experiments (Polet et al., 2000) as shown in Fig. 1. (b) Results from local S phases (see Fig. 3) are more heterogeneous.

(Savage, 1999; Rumpker and Silver, 1998). In addition, extreme delay times can be obtained from the splitting-parameter grid search when anisotropy is virtually absent as indicated by the elongated 95% confidence regions (Silver and Chan, 1991).

We compare our observations along the northern profile with results obtained from single S phases of local events that occurred within the slab at depths between 150 and 350 km beneath the Altiplano plateau. We do not apply the joint-splitting approach to local phases due to the strong variation of initial polarization directions along the profile and with respect to the high probability of anisotropic patterns changing with depth. Detailed splitting parameters are given in the Supplementary Table S5. The delay times are smaller than those obtained from SKS phases and range between 0.13 and 1.08 s (Fig. 3). The corresponding fast polarizations show much higher variability compared to the SKS results. Fast directions in the vicinity of major fault zones tend to be aligned more or less parallel to the strike of the faults (Fig. 3). The largest delay times are again observed in the Altiplano plateau which coincides with the observations from SKS splitting analysis. Due to the lack of deep earthquakes in that region we are not able to determine splitting parameters from local S phases along the Puna profile. A comparison of the resulting splitting parameters from SKS and local S phases reveals differing distributions of fast-axis polarizations (Fig. 4) with SKS results clearly dominated by EW directions. In contrast, fast polarizations from local events exhibit a much higher variability with a tendency to N and NE–SW trending orientations.

3. Waveform modeling

We assess the influence of different anisotropic regions on SKS phases using wavefield modeling based on a 2-dimensional explicit finite-difference (FD) approximation of the complete elastic wave equation (Ryberg et al., 2002). Splitting parameters are determined from computed synthetic waveforms and are then compared with the observed SKS splitting along the Altiplano profile. In our modeling we consider wave propagation within a vertical (x_1 – x_3) plane, where x_1 denotes the horizontal axis and x_3 the vertical axis. We assume that material properties and the wave field are invariant in the x_2 direction oriented parallel to the trench. Anisotropy in the mantle is assumed to originate from crystallographic preferred orientation (CPO) of orthorhombic olivine crystals such that the elastic tensor can be characterized by nine independent elastic constants (Kumazawa and Anderson, 1969). We use an average crustal thickness of 60 km and assume the lower boundary of the lithosphere at a depth of 80 km as previously derived from receiver functions (Wölbern et al., 2009). The slab dip is taken from investigations of the local seismicity (Cahill and Isacks, 1992). Fig. 5 displays the general setup of the anisotropic velocity model. In order to suppress side effects, such as artificial reflections from the grid boundaries, the grid was chosen much larger than the evaluated lateral region of 600 km. Free-surface conditions were specified at the upper boundary ($x_3 = 0$) of the computational grid. Below 400 km we assume the material to be isotropic in accordance with the proposed transition from dislocation creep to

diffusion creep (Fouch and Rondenay, 2006; Meade et al., 1995). A plane vertically-propagating shear wavefront is initialized in this isotropic region with an initial source polarization matching the backazimuth of the analyzed SKS data. The grid spacing is chosen to be 250 m. Within the slab, the fast axis of the model is assumed to align parallel to the direction of slab motion (according to A-type olivine). At 21°S the strike of the Nazca slab differs by about -10° from the North direction. Accordingly, the observed fast polarizations have been rotated clockwise to enable comparison with the results of the synthetic data, i.e. in Figs. 6 and 7 we add 10° to the observed Φ . Results obtained from local slab events are not considered in the modeling mainly due to the different frequency content. SKS phases are dominated by rather long periods. Accordingly, synthetic waveforms are computed with a dominant period of 8 s. The local S phases analyzed in this study exhibit a dominant period of 1–2 s and are, therefore, much more affected by small scale structures that are not resolved by SKS phases. Consequently, splitting parameters derived from both data sets are not expected to be comparable.

A summary of all models discussed in this study is given in Table 1. The first model (Fig. 6a) incorporates only trench-parallel fast axes in the mantle beneath the slab in accordance with previously derived models of the flow field. We assume 4.5% anisotropy to obtain delay times approximately as large as inferred from source-side splitting analysis (Russo and Silver, 1994). For this model, theoretical delay times decrease towards the east due to the thinning of the anisotropic layer as the anisotropy dissolves beneath 400 km. To compensate for this effect, an extreme increase of anisotropic strength of up to 15% would be required beneath the slab to explain the delay times observed from source-side splitting. In order to simultaneously explain our SKS results for such a model the fast polarization due to sub-slab anisotropy needs to be overprinted. For example, as much as 10% anisotropy in the slab would be required to explain the observed SKS delay times at the westernmost stations (Fig. 6b). However, the effects related to thinning of the anisotropic layer in the sub-slab mantle still persist. For compensation, anisotropy within the slab would also be required to decrease towards the east which we consider to be unrealistic. We further test a model with 1.5% “frozen-in” anisotropy in the slab only (Supplementary Fig. S4). In this case the theoretical and observed SKS splitting results agree well along the first 300 km of the profile. However, to compensate for a slight mismatch of the fast-polarization directions additional anisotropy (4.5%) is assumed in the continental crust with a fast axis orientation of -11° with respect to the strike of the trench. At the same time, the strength of slab anisotropy needs to be increased to 3.8% to explain the observed delay times (Fig. 6c). To fit the splitting parameters along the eastern half of the profile we further include two anomalous blocks in the mantle wedge (Fig. 6d). However, the model is not capable of reproducing the observed EW orientations between the two anomalies indicated earlier (at about 400 km along the profile), likely because the resulting SKS Fresnel zones at that depths are too large to resolve these short-scale structures (Rumpker and Ryberg, 2000; Hanna and Long, 2012).

A much better fit to the data is obtained by assuming isolated anisotropic anomalies (11% and 7.5%) within the crust (Fig. 7a). The comparison between the theoretical and observed splitting parameters shows that the shallow origin of the anisotropy allows to account for the abrupt changes of the fast directions and the delay times. Additional uniform anisotropy within the whole mantle wedge does not improve the fit of the data (Supplementary Fig. S5). According to laboratory experiments on subduction zone rheology the mineral alignment within the wedge is likely limited to regions directly above the slab and below the continental lithosphere (Buttles and Olson, 1998). Related anisotropic effects may be accounted for by varying the thickness of the

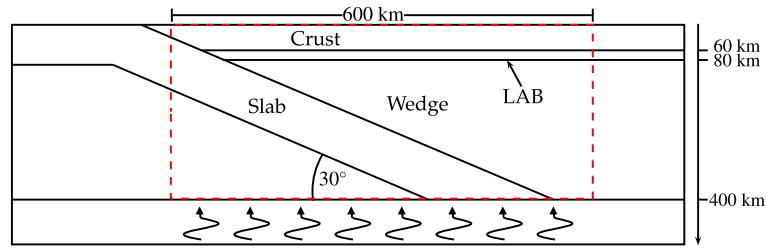


Fig. 5. Schematic vertical cross section (taken parallel to the direction of plate motion) of the 2-dimensional subduction zone model as used in the waveform computations. The incident waveform is initialized at a depth below 400 km, where the mantle is assumed to be isotropic. The dashed line marks the range for which splitting parameters are obtained.

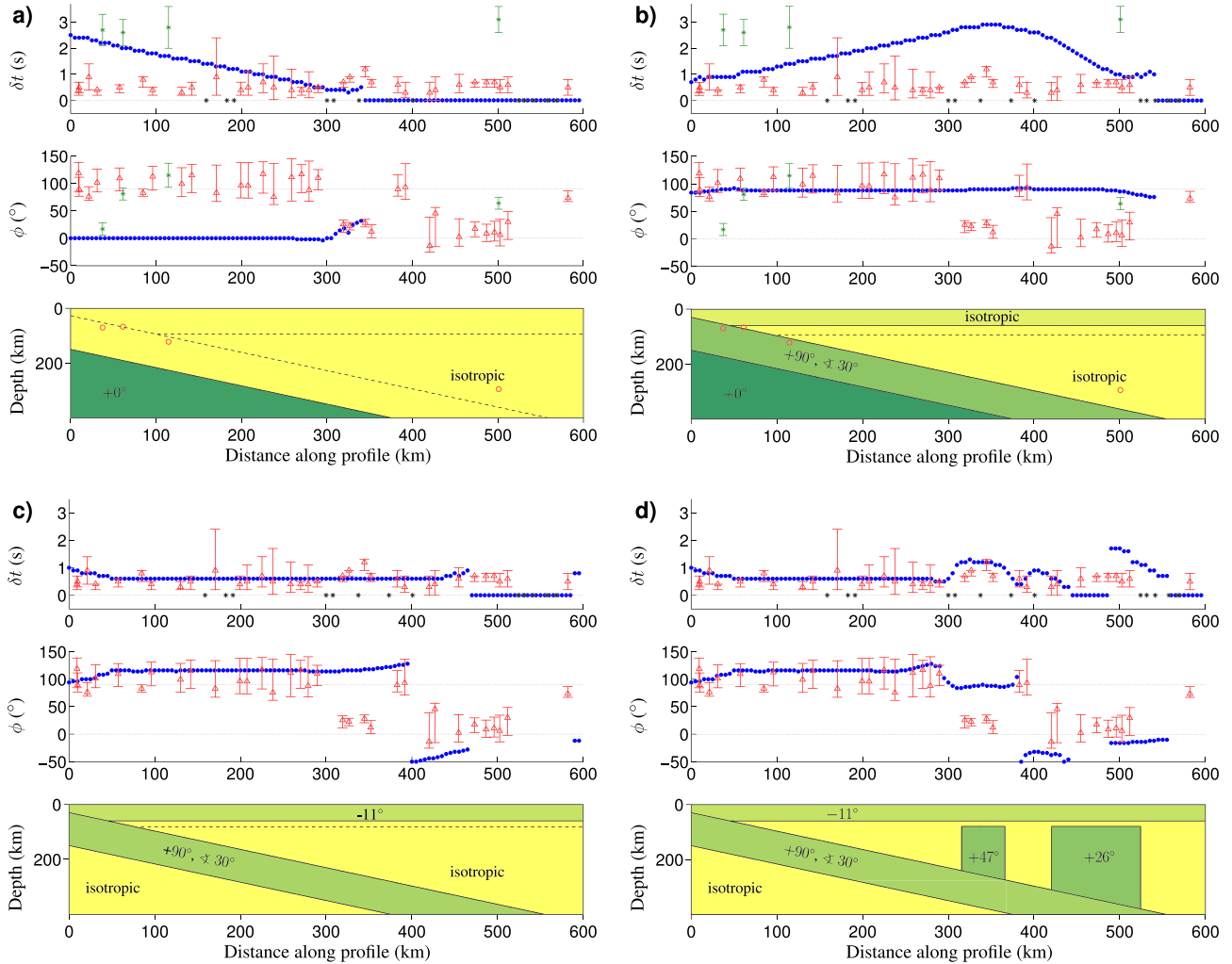


Fig. 6. Anisotropic subduction-zone models (lower panels) and comparison of observed (red triangles; black asterisks denote null measurements) and theoretical (blue dots) splitting parameters (upper panels) obtained from FD waveform modeling for the northern profile. Models display trench-normal vertical cross-sections, where 0° refers to the strike of the subducting slab which deviates by -10° from the north at this latitude. The observed fast polarizations are adjusted accordingly by clockwise rotation. Negative and positive numbers indicate western and eastern orientations of the fast (symmetry) axes in the models, respectively. (a) Trench-parallel anisotropy only (4.5%) restricted to the sub-slab (dark green). Green dots denote previous results (Russo and Silver, 1994), red circles mark epicenters of related slab earthquakes. (b) Additional fossil slab anisotropy (10%) with fast axis parallel to the plate motion. (c) 3.8% fossil slab anisotropy parallel to the Nazca plate motion combined with 4.5% crustal anisotropy with the fast axis pointing towards -11° with respect to the strike of the trench, i.e. N21°W. (d) The same model with two additional anomalies (1.5% and 0.5%) in the mantle wedge with fast-axis orientations pointing towards $+47^\circ$ and $+26^\circ$ relative to the strike of the trench, respectively (i.e. N37°E and N16°E).

oceanic lithosphere or the amount of slab anisotropy in our model. The same applies to a possible contribution from mantle flow beneath the Nazca slab and also to hypothesized serpentine deformation in the hydrated mantle wedge (Katayama et al., 2009; Jung, 2011) or within the subducting slab (Faccenda et al., 2008), as long as the resulting direction of the fast axis is either parallel or perpendicular to that of the Nazca plate movement. We have

further considered the existence of B-type olivine under water-rich conditions (Jung et al., 2009; Ohuchi et al., 2012), which generates fast-axis orientations perpendicular to the plate motion. Its occurrence is most likely restricted to the fore-arc region (Ohuchi et al., 2012) and the effect on our results is marginal (Fig. 7b). A corresponding zone of trench-parallel anisotropy may provide a possible explanation for the observed null measurements at about

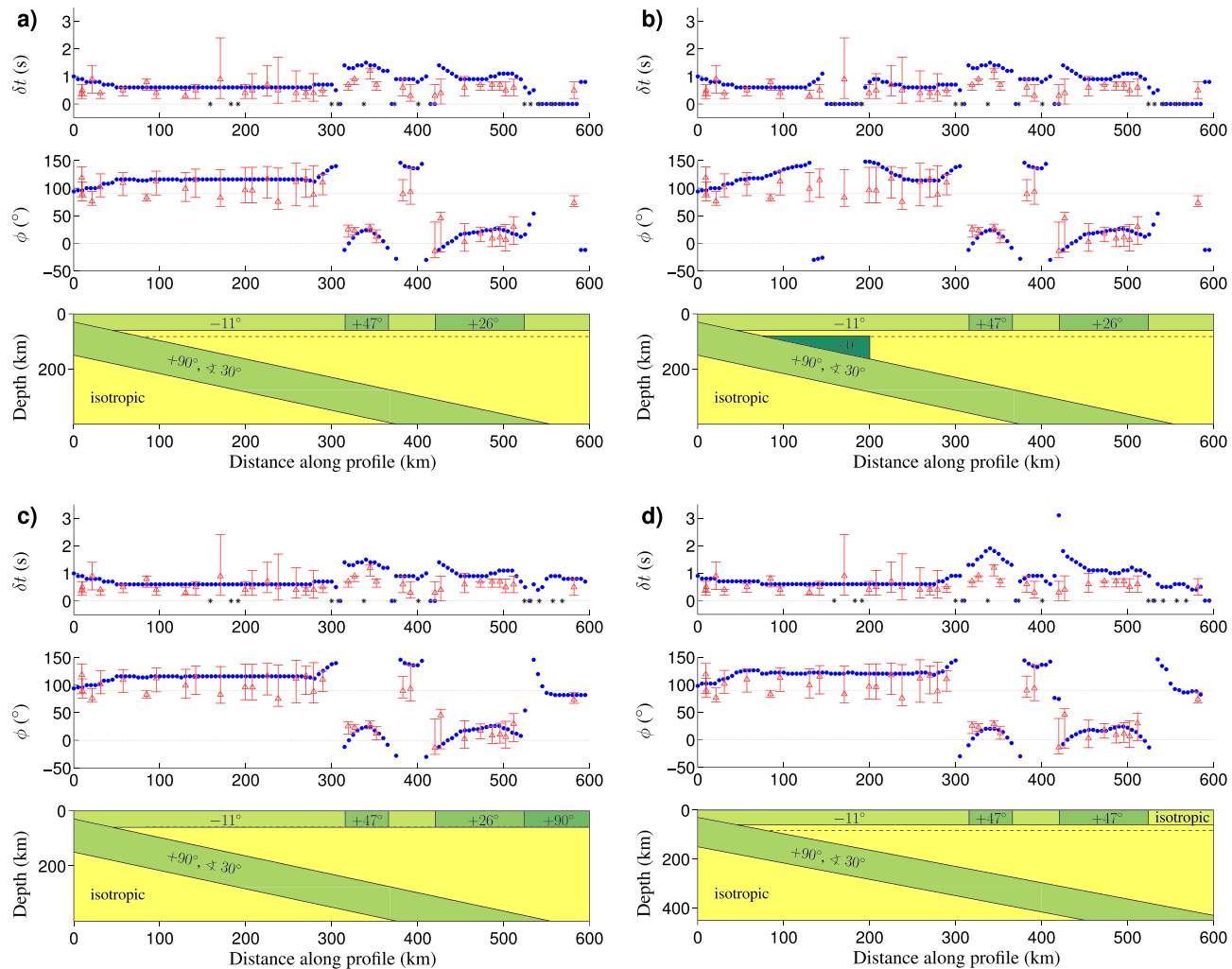


Fig. 7. Improved anisotropic subduction-zone models and resulting splitting parameters. Symbols and illustrations are the same as in Fig. 6. (a) Model with slab and crustal anisotropy as given in Fig. 6c with additional crustal anomalies (11% and 7.5%). The corresponding fast-axis directions are the same as in Fig. 6d. (b) Additional B-type olivine (7% anisotropy) with fast-axis parallel to the trench in the mantle wedge from the slab contact to the volcanic arc. (c) Adjustment of the observed fast polarization at the easternmost station by an additional crustal block (3%) with fast axis aligned towards +90° with respect to the trench (i.e. N80°E). (d) An alternative model assumes fossil slab anisotropy (4.5%) persisting below 400 km depth. The easternmost segment of the crust is assumed to be isotropic.

Table 1
Summary of models presented in this study. Each row represents one model. In columns, the different layers and units are characterized by means of the strength of anisotropy and the fast-axis directions with respect to the strike of the trench.

#	Sub-slab	Slab ^{a,b}	Wedge	Crust	Block 1 ^c	Block 2 ^c	Block 3 ^d	Fig.
1	4.5%; ±0°	isotropic	isotropic	isotropic	–	–	–	6a
2	4.5%; ±0°	10%; +90°	isotropic	isotropic	–	–	–	6b
3	isotropic	1.5% +90°	isotropic	isotropic	–	–	–	S4
4	isotropic	3.8%; +90°	isotropic	4.5%; –11°	–	–	–	6c
5	isotropic	3.8%; +90°	isotropic	4.5%; –11°	1.5%; +47°	0.5%; +26°	–	6d
6	isotropic	3.8%; +90°	isotropic	4.5%; –11°	11.0%; +47°	7.5%; +26°	–	7a
7	isotropic	3.8%; +90°	1.0%; +90	4.5%; –11°	11.0%; +47°	7.5%; +26°	–	S5
8	isotropic	3.8%; +90°	isotropic	4.5%; –11°	11.0%; +47°	7.5%; +26°	7.0%; ±0°	7b
9	isotropic	3.8%; +90°	isotropic	4.5%; –11°	11.0%; +47°	7.5%; +26°	3.0%; +90°	7c
10	isotropic	3.8%; +90°	isotropic	4.5%; –11°	12.0%; +47°	10.0%; +26°	isotropic	7d

^a The fast-axis within the slab is tilted by 30° in all models according to the slab dip.
^b Slab anisotropy terminates at 450 km depth in model 10, but, at 400 km in all other models.
^c In model 5 the anomalous blocks 1 and 2 are located in the mantle wedge. In models 6–10 these anomalies are situated in the continental crust.
^d In model 8 anomalous block 3 represents B-type olivine restricted to the fore-arc wedge. In model 9 an additional crustal anomaly is considered at the easternmost part of the profile.

170–200 km along the profile while, at the same time, it reduces the fit of the fast polarizations observed at adjacent locations. Our observations are best explained by assuming 7% anisotropy of the B-type fabric in the fore-arc mantle wedge. If the anisotropy were assumed to be slightly stronger, null measurements would occur

over a wider range at the surface. If the strength of anisotropy were to be increased further, the theoretical fast polarizations would turn towards NS directions.
The easternmost station of the profile exhibits an EW oriented fast polarization which is in conflict with our model (Fig. 7a). Here,

the slab sinks below 400 km depth where anisotropy is assumed to terminate (Fouch and Rondenay, 2006; Meade et al., 1995) and, therefore, theoretical waveforms only reflect the crustal anisotropy. The EW fast polarization can be explained equally well by two different models. The first includes 3% crustal anisotropy with a fast-axis orientation near-parallel to the Nazca plate motion (Fig. 7c). However, this specific pattern of anisotropy is not related to any known geological structure in that area. Alternatively, the observed fast polarizations can be explained by fossil slab anisotropy if it persists to even greater depth possibly preserved by the lower slab temperatures relative to the ambient mantle. As in the previous models we assume 3.8% and 4.5% anisotropy within the slab and the crust, respectively. In this model, the easternmost segment of the crust is assumed to be isotropic to better explain the observed fast polarizations. However, the continuation of slab anisotropy to greater depths also affects the splitting parameters related to the crustal anomalies. The best fit to the observed splitting parameters is obtained assuming fast-axis directions of $+47^\circ$ with respect to the strike of the Nazca slab (i.e. N37°E) and strengths of anisotropy of 12% and 10%, respectively (Fig. 7d).

4. Discussion and conclusions

We have investigated lateral variations of shear-wave splitting in the Central Andes based on SKS and local S phases. Splitting parameters from the joint-splitting analysis are in good agreement with the results from individual events and are less affected by noise. We have successively evaluated effects of different anisotropic regions on the splitting parameters by comparison with results from full-waveform FD-modeling. The observed dominating EW directions of the fast-polarizations in the Central Andes coincide with relatively uniform delay times. This likely indicates that the anisotropy originates from a layer of relatively uniform thickness. The prevailing EW polarizations can be explained by 3.8% fossil slab anisotropy with a fast axis sub-parallel to the direction of the Nazca plate motion. Our preferred model further indicates a significant crustal component of anisotropy (4.5%) with a fast axis of approximately N21°W. A possible source for this alignment is provided by ductile flow in the lower crust from the Puna towards the Altiplano plateau as previously suggested from geodynamic modeling to explain the different accommodation rates in these two regions (Gerbault et al., 2005). According to their numerical models this crustal flow is induced by heterogeneous densities in the mantle which causes a mass transfer towards the north that is confined to the highly elevated plateaus and terminates east of which. This would also explain the apparent absence of crustal anisotropy in the easternmost part of the crust as demonstrated in our model shown in Fig. 7d. Due to the limited depth range of this flow field between 20 km and 65 km the crustal component of anisotropy is supposed to be slightly stronger than the 4.5% assumed in our model which incorporates the entire crust. An additional component of crustal anisotropy is in agreement with results from receiver functions: Leidig and Zandt (2003) have presented models assuming up to 30% anisotropy within the upper crust possibly due to a system of fluid-filled cracks in the context of the Altiplano–Puna volcanic complex. However, our results do not allow to distinguish between these mechanisms; a combination of the effects is also possible.

The largest delay times along the northern profile for both SKS and local S phases are related to confined zones where fast polarizations deviate from the general trench-normal orientations. A large number of fast polarizations, especially those obtained from local events, are oriented sub-parallel to the strike directions of major fault systems (Elger et al., 2005; ANCORP Working Group, 2003) as shown in Fig. 3. In the Altiplano region, the anomalous fast polarizations in the crust align sub-parallel to the trend of

the Uyuni–Kenayani fault zone (Fig. 3). The western edge of the second crustal anomaly roughly coincides with the location of the San Vicente Fault Zone (Fig. 3). From our modeling it seems likely that the relatively short-scale lateral variations are mainly due to crustal influences (Rümpker and Ryberg, 2000) possibly connected to the major fault systems. These faults appear to have a significant impact on the observed splitting results and seem to overprint the anisotropic signature of the lower crustal ductile flow suggested above. Small-scale lateral variations of shear-wave splitting can also originate from strong variations of isotropic velocities (Kaviani et al., 2011) which may provide an alternative or additional explanation for the observed anomalies. However, strong small-scale velocity variations, such as thick sedimentary basins, are not considered likely to exist in the Central Andes and have, therefore, not been included in our models. Although our study does not rule out the existence of trench-parallel flow beneath the slab we believe that complex anisotropy in the crust, probably a combination of ductile deformation in the lower crust and effects of aligned fault-systems, provides a more likely explanation for the observed variations in splitting parameters.

Acknowledgements

I. Wölbern was financially supported (WO 1723/1-1) by Deutsche Forschungsgemeinschaft (DFG). We thank the GEOFON data center at GFZ Potsdam for providing the waveform data used in this study. The ReFuCA project was funded by Deutsche Forschungsgemeinschaft (DFG) within the Collaborative Research Center SFB-267. We appreciate the fieldwork performed by G. Asch and co-workers. Results and maps were visualized with the GMT software (Wessel and Smith, 1998). The manuscript significantly benefited from the constructive comments and suggestions of two anonymous reviewers.

Appendix A. Supplementary material

Supplementary material related to this article can be found online at <http://dx.doi.org/10.1016/j.epsl.2014.02.032>.

References

- ANCORP Working Group, 2003. Seismic imaging of a convergent continental margin and plateau in the central Andes (Andean Continental Research Project 1996 (ANCORP '96)). *J. Geophys. Res.* 108, 2328. <http://dx.doi.org/10.1029/2002JB001771>.
- Bock, G., Kind, R., Rudloff, A., Asch, G., 1998. Shear wave anisotropy in the upper mantle beneath the Nazca plate in northern Chile. *J. Geophys. Res.* 103, 24333–24345.
- Buontempo, L., Wuestefeld, A., 2012. Complex fault structure interactions of crustal shear zones revealed by seismic anisotropy: an example in the eastern betic cordillera (Spain). *Terra Nova* 25, 57–64.
- Buttles, J., Olson, P., 1998. A laboratory model of subduction zone anisotropy. *Earth Planet. Sci. Lett.* 164, 245–262.
- Cahill, T., Isack, B.L., 1992. Seismicity and shape of the subducted Nazca plate. *J. Geophys. Res.* 97, 17503–17529.
- Di Leo, J.F., Wookey, J., Hammond, J.O.S., Kendall, J.-M., Kaneshima, S., Inoue, H., Yamashina, T., Harjadi, P., 2012. Deformation and mantle flow beneath the Sangihe subduction zone from seismic anisotropy. *Phys. Earth Planet. Inter.* 194–195, 38–54.
- Elger, K., Oncken, O., Glodny, J., 2005. Plateau-style accumulation of deformation: Southern Altiplano. *Tectonics* 24, TC4020. <http://dx.doi.org/10.1029/2004TC001675>.
- Faccenda, M., Burlini, L., Gerya, T.V., Mainprice, D., 2008. Fault-induced seismic anisotropy by hydration in subducting oceanic plates. *Nature* 455, 1097–1101.
- Fischer, K.M., Parmentier, E.M., Stine, A.R., Wolf, E.R., 2000. Modeling anisotropy and plate-driven-flow in the Tonga subduction zone back arc. *J. Geophys. Res.* 105, 16181–16191.
- Fouch, M.J., Rondenay, S., 2006. Seismic anisotropy beneath stable continental interiors. *Phys. Earth Planet. Inter.* 158, 292–320.
- Gerbault, M., Martinod, J., Hérail, G., 2005. Possible orogeny-parallel lower crustal flow and thickening in the Central Andes. *Tectonophysics* 399, 59–72.

- Hammond, J.O.S., Wookey, J., Kaneshima, S., Inoue, H., Yamashina, T., Harjadi, P., 2010. Systematic variation in anisotropy beneath the mantle wedge in the Java–Sumatra subduction system from shear-wave splitting. *Phys. Earth Planet. Inter.* 178, 189–201.
- Hanna, J., Long, M.D., 2012. SKS splitting beneath Alaska: Regional variability and implications for subduction processes at a slab. *Tectonophysics* 530–531, 272–285.
- Heit, B., Koulakov, I., Asch, G., Yuan, X., Kind, R., Alcozer-Rodriguez, I., Tawackoli, S., Wilke, H., 2008. More constraints to determine the seismic structure beneath the Central Andes at 21°S using teleseismic tomography analysis. *J. South Am. Earth Sci.* 25, 22–36.
- Homuth, B., 2010. SKS-Splitting und seismische Anisotropie in der Rhenan-Region, Ostafrikanisches Rift. Master thesis. Goethe-Universität Frankfurt (in German).
- Jung, H., 2011. Seismic anisotropy produced by serpentine in mantle wedge. *Earth Planet. Sci. Lett.* 307, 535–543.
- Jung, H., Karato, S., 2001. Water-induced fabric transition in olivine. *Science* 293, 1460–1463.
- Jung, H., Mo, W., Green, H.W., 2009. Upper mantle seismic anisotropy resulting from pressure-induced slip transition in olivine. *Nat. Geosci.* 2, 73–77.
- Katayama, I., Karato, S., 2006. Effect of temperature on the B- to C-type olivine fabric transition and implication for flow pattern in subduction zones. *Phys. Earth Planet. Inter.* 157, 33–45.
- Katayama, I., Hirauchi, K., Michibayashi, K., Ando, J., 2009. Trench-parallel anisotropy produced by serpentine deformation in the hydrated mantle wedge. *Nature* 461, 1114–1118.
- Kavianian, A., Rumpker, G., Weber, M., Asch, G., 2011. Short-scale variations of shear-wave splitting across the Dead Sea basin: Evidence for effects of sedimentary fill. *Geophys. Res. Lett.* 38, L04308. <http://dx.doi.org/10.1029/2010GL046464>.
- Kneller, E.A., van Keken, P.E., 2007. Trench-parallel flow and seismic anisotropy in the Mariana and Andean subduction systems. *Nature* 450, 1222–1225.
- Kumazawa, M., Anderson, O.L., 1969. Elastic moduli, pressure derivatives, and temperature derivatives of single-crystal olivine and single-crystal forsterite. *J. Geophys. Res.* 74, 5961–5972.
- Leidig, M., Zandt, G., 2003. Modeling of highly anisotropic crust and application to the Altiplano–Puna volcanic complex of the Central Andes. *J. Geophys. Res.* 108, 2003. <http://dx.doi.org/10.1029/2001JB000649>.
- Liu, K.H., Gao, S.S., Gao, Y., Wu, J., 2008. Shear wave splitting and mantle flow associated with the deflected Pacific slab beneath northeast Asia. *J. Geophys. Res.* 113, B01305. <http://dx.doi.org/10.1029/2007JB005178>.
- Long, M.D., Silver, P.G., 2008. The subduction zone flow field from seismic anisotropy: A global view. *Science* 319, 315–318.
- Long, M.D., Silver, P.G., 2009a. Shear wave splitting and mantle anisotropy: measurements, interpretations, and new directions. *Surv. Geophys.* 30, 407–461.
- Long, M.D., Silver, P.G., 2009b. Mantle flow in subduction systems: The subslab flow field and implications for mantle dynamics. *J. Geophys. Res.* 114, B10312. <http://dx.doi.org/10.1029/2008JB006200>.
- Lynner, C., Long, M.D., 2013. Sub-slab seismic anisotropy and mantle flow beneath the Caribbean and Scotia subduction zones: Effects of slab morphology and kinematics. *Earth Planet. Sci. Lett.* 361, 367–378.
- Meade, C., Silver, P.G., Kaneshima, S., 1995. Laboratory and seismological observations of lower mantle isotropy. *Geophys. Res. Lett.* 22, 1293–1296.
- Ohuchi, T., Kawazoe, T., Nishihara, Y., Nishiyama, N., Irifune, T., 2011. High pressure and temperature fabric transitions in olivine and variations in upper mantle seismic anisotropy. *Earth Planet. Sci. Lett.* 304, 55–63.
- Ohuchi, T., Kawazoe, T., Nishihara, Y., Irifune, T., 2012. Change of olivine a-axis alignment induced by water: Origin of seismic anisotropy in subduction zones. *Earth Planet. Sci. Lett.* 317–318, 111–119.
- Park, J., Levin, V., 2002. Seismic anisotropy: tracing plate dynamics in the mantle. *Science* 296, 485–489.
- Polet, J., Silver, P.G., Beck, S., Wallace, T., Zandt, G., Ruppert, S., Kind, R., Rudloff, A., 2000. Shear wave anisotropy beneath the Andes from BANJO, SEDA, and PISCO experiments. *J. Geophys. Res.* 105, 6287–6304.
- Rabbet, W., Kaban, M., Tesaro, M., 2013. Contrasts of seismic velocity, density and strength across the Moho. *Tectonophysics* 609, 437–455.
- Restivo, A., Helffrich, G., 1999. Teleseismic shear wave splitting measurements in noisy environments. *Geophys. J. Int.* 137, 821–830.
- Rümpker, G., Ryberg, T., 2000. New “Fresnel-zone” estimates for shear-wave splitting observations from finite-difference modeling. *Geophys. Res. Lett.* 27, 2005–2008.
- Rümpker, G., Silver, P.G., 1998. Apparent shear-wave splitting parameters in the presence of vertically varying anisotropy. *Geophys. J. Int.* 135, 790–800.
- Russo, R.M., Silver, P.G., 1994. Trench-parallel flow beneath the Nazca plate from seismic anisotropy. *Science* 263, 1105–1111.
- Ryberg, T., Rümpker, G., Tittgemeyer, M., Wenzel, F., 2002. Finite-difference simulations of seismic wavefields in isotropic and anisotropic Earth models. In: Krause, E., Jäger, W. (Eds.), *High Performance Computing in Science and Engineering 2001*. Springer-Verlag, Berlin, Heidelberg, pp. 35–47.
- Savage, M.K., 1999. Seismic anisotropy and mantle deformation: What have we learned from shear wave splitting? *Rev. Geophys.* 37, 65–106.
- Silver, P.G., Chan, W.W., 1991. Shear wave splitting and subcontinental mantle deformation. *J. Geophys. Res.* 96, 16429–16454.
- Teanby, N.A., Kendall, J.-M., van der Baan, M., 2004. Automation of shear-wave splitting measurements using cluster analysis. *Bull. Seismol. Soc. Am.* 94, 453–463.
- Tono, Y., Fukao, Y., Kunugi, T., Tsuboi, S., 2009. Seismic anisotropy of the Pacific slab and mantle wedge beneath the Japanese islands. *J. Geophys. Res.* 114, B07307. <http://dx.doi.org/10.1029/2009JB006290>.
- Vinnik, L.P., Farra, V., Romanowicz, B., 1989. Azimuthal anisotropy in the Earth from observations of SKS at Geoscope and NARS broadband stations. *Bull. Seismol. Soc. Am.* 79, 1542–1558.
- Wessel, P., Smith, W.H.F., 1998. New, improved version of the Generic Mapping Tools released. *Eos Trans. AGU* 79, 579.
- Wölbern, I., Heit, B., Yuan, X., Asch, G., Kind, R., Viramonte, J., Tawackoli, S., Wilke, H., 2009. Receiver function images from the Moho and the slab beneath the Altiplano and Puna plateaus in the Central Andes. *Geophys. J. Int.* 177, 296–308.
- Wolfe, C.J., Silver, P.G., 1998. Seismic anisotropy of oceanic upper mantle: Shear wave splitting methodologies and observations. *J. Geophys. Res.* 103, 749–771.
- Wüstefeld, A., Bokelmann, G., Zaroli, C., Barruol, G., 2008. SplitLab: A shear-wave splitting environment in Matlab. *Comp. Geosci.* 34, 515–528.